Best, S. R., Croxford, A. J., & Neild, S. A. (2014). Modelling harmonic generation measurements in solids. Ultrasonics, 54(2), 442-450. 10.1016/j.ultras.2013.05.012

Modelling Harmonic Generation Measurements in Solids

S.R. Best*, A.J. Croxford, S. A. Neild

Department of Mechanical Engineering, Queen's Building, University Walk, Bristol, BS8 1TR, UK

Abstract

Harmonic generation measurements typically make use of the plane wave result when extracting values for the nonlinearity parameter, β, from experimental measurements. This approach, however, ignores the effects of diffraction, attenuation, and receiver integration which are common features in a typical experiment. Our aim is to determine the importance of these effects when making measurements of β over different sample dimensions, or using different input frequencies. We describe a three-dimensional numerical model designed to accurately predict the results of a typical experiment, based on a quasi-linear assumption. An experiment is designed to measure the axial variation of the fundamental and second harmonic amplitude components in an ultrasonic beam, and the results are compared with those predicted by the model. The absolute β values are then extracted from the experimental data using both the simulation and the standard plane wave result. A difference is observed between the values returned by the two methods, which varies with axial range and input frequency.

Keywords: Harmonic generation, Sound beam, Aluminium

1. Introduction

Effective damage detection methods are of vital importance to the ageing power plants used in the nuclear industry. Nonlinear ultrasonics represent a means of monitoring damage in metallic components which are routinely subject to demanding operating conditions. Under such conditions, metals are known to undergo fatigue mechanisms which lead, through the accumulation of dislocations, to microcrack initiation, and ultimately terminal cracking. In the early stages,

*Corresponding author
Email address: mesrb@bristol.ac.uk (S.R. Best)

before any cracks or voids have materialised, there are nonetheless changes in the bulk properties of the material. One such property is the nonlinear response of the material, which is a quantity related to the third-order elastic constants. Through the use of nonlinear ultrasonics, we are able to measure changes in a material's nonlinear response, and therefore track the onset of early-stage damage.

The nonlinear harmonic generation technique makes use of the acoustic nonlinear parameter, β, which is related to the third-order elastic constants of the material as follows (Beyer, 1998) [1]:

$$\beta = -\left(\frac{3}{2} + \frac{\mathcal{A} + 3\mathcal{B} + \mathcal{C}}{\rho_0 c_l^2}\right) \tag{1}$$

where ρ_0 is the equilibrium density of the solid, c_l is the longitudinal sound speed, and $\mathcal{A}$, $\mathcal{B}$, $\mathcal{C}$ are the third order elastic constants of Landau and Lifshitz [2]. Note that this value of β is a factor of two smaller than the version often quoted (e.g. [3, 4, 5]) for solids, a fact also recently noted by Pantea et al. [6]. Eq. (1) is shown to be consistent with the nonlinear parameter for fluids when the equivalent constants are used [1], and it is the definition of β used throughout this paper.

Currently, most practical attempts to measure the nonlinearity of solids, e.g. [7, 8, 9, 10], have made use of the plane wave theory of nonlinear elasticity to derive a means of calculating β from experimental measurements. The resulting expression is that derived by Zarembo and Krasil'nikov (1971) [3]:

$$\beta = \frac{4}{k^2 x}\frac{A_2}{A_1^2} \tag{2}$$

Here a single-frequency continuous excitation at the source is assumed, with wave number k. A_1 and A_2 represent the displacement amplitudes of the first and second harmonic components of the captured signal, and x is the propagation distance. In the case of non-zero attenuation in the material, Eq. (2) is modified to:

$$\beta = \frac{8\alpha}{k^2(1 - e^{-2\alpha x})}\frac{A_2}{A_1^2} \tag{3}$$

where α is the attenuation value at the fundamental frequency. Note that Eq. (3) assumes a thermoviscous damping law, whereby the attenuation value at the second harmonic is four times that at the fundamental frequency. Liu et al. [11] recently made use of this result to measure nonlinearity in a fatigued aluminium specimen, and also applied a correction for a windowed excitation.

The issue with using Eqs. (2) and (3) to measure β is that they are based on a plane wave assumption, and do not fully account for the behaviour of the acoustic field. Considering a typical experimental set up, a transmitting device is normally required to generate an ultrasonic signal in the specimen. This is often a circular transducer coupled to the surface of the specimen, and at the frequencies generally used for ultrasonic measurements (1-50MHz), the acoustic field emitted from such a source is likely to exhibit diffraction. This produces complex pressure patterns in the acoustic field, which vary with transducer size, input frequency, and propagation distance. An additional consideration is the receiving transducer used for a measurement. in the case of a non-planar incident field, the received signal is an average over the finite area of the receiver. Depending on the receiver size, therefore, the averaged amplitude can differ greatly to that which would be measured by a point receiver; that is, the actual physical amplitude. Under these circumstances, it is therefore questionable whether either of Eqs. (2) and (3) can be used to make accurate measurements of absolute β. This may also apply to the case in which relative measurements of β are required, but using different transducer sizes, input frequencies, or sample dimensions.

These issues have received limited attention in the literature. Earlier, Blackburn & Breazeale [12] corrected for the combined effects of field diffraction and receiver integration when making nonlinearity measurements in small samples. This combined correction, referred to as the diffraction correction, was derived by Rogers & Van Buren [13] by calculating the integrated amplitude of the linear field over the receiving transducer surface. However, this could only be accurately applied to the fundamental amplitudes, leaving the second harmonic amplitudes uncorrected. A further instance of correcting for diffraction is the work by Hurley & Fortunko [4], who used a similar correction to Rogers & Van Buren for the linear field, and included an additional approximate correction for the second harmonic. More recently, in the field of fluids, both Labat et al. [14] and Chavrier et al. [15] used numerical models of sound beam propagation to make nonlinearity measurements. In doing this, the model parameters were matched to those of the experiment, and the predicted trends were scaled to match the experimental results.

In this paper we develop a simulation intended to capture all of the variables associated with a typical harmonic generation measurement. These are the nonlinearity, diffraction and attenuation in the sound beam, as well as the integration of the receiver. We describe a sound beam model based on a quasi-linear assumption, which is similar to a solution of the Khokhlov-Zabolotskaya-Kuznetsov (KZK) equation [16]. The model is then augmented with a formula to calculate the receiver integration. Our overall aim is to determine the importance of the combined effects when measuring nonlinearity, when compared to the standard plane wave measurement. We devise an experiment to measure the axial variation of the fundamental and second harmonic in the vicinity of a real source, and compare the trends with those predicted by the simulation. The simulated results are then used to extract absolute β from the experimental data, which enables a comparison to be made with the corresponding values derived using the plane wave result.

2. Numerical model

The metallic materials of interest in non-destructive evaluation are known to exhibit low levels of nonlinearity. A typical harmonic generation measurement, for example, may show second harmonic signals which are up to three orders of magnitude smaller than the fundamentals. In these physical circumstances, it is valid to employ the quasi-linear approximation for modelling, which deals with nonlinearity using a perturbation approach. The fundamental response is captured by linear analysis, the second harmonics then satisfy the nonlinear wave equation when the linear terms are used as a forcing. The physical mechanism of nonlinear generation in the quasi-linear approximation is treated as the emission of a second-order wave from each point in the domain of linear wave propagation. This is visualised as a field of virtual sources, the amplitude of each source being proportional to the square of the local first-order amplitude. To calculate the second-order field at a given point in a sound beam therefore requires integration over all sources in the three dimensional space. An early mathematical expression of this was reported by Ingenito and Williams (1971) [17]:

$$u_2(x,y,z) = C\int_0^Z \int_{-Y}^{Y} \int_{-X}^{X} u_1^2(x',y',z')G(x,y,z|x',y',z')dx'dy'dz' \tag{4}$$

Here, $u_2(x,y,z)$ is the second-order velocity amplitude at a point with Cartesian position coordinates with respect to the centre of the source, z being the direction of propagation. $u_1(x',y',z')$ is the local linear amplitude associated with a virtual source, which has volume $dx'dy'dz'$. The

$G(x, y, z|x', y', z')$ terms are the Green's functions which describe the propagation from the virtual source to the target point:

$$G = (1/R)\exp(2ikR - \alpha_2 R) \tag{5}$$

where α_2 is the attenuation coefficient at the second harmonic frequency, and

$$R = [(x - x')^2 + (y - y')^2 + (z - z')^2]^{(1/2)} \tag{6}$$

is the distance from the virtual source to the target. The constant C in Eq. (4) is determined by swapping the fluid nonlinear parameter given in [17] for that associated with solids, giving $C = k^2\beta/(2\pi c)$. Note that this switch treats longitudinal wave propagation in solids as being similar to that in liquids; that is, it ignores any mode conversion in the solid. This is a reasonable assumption for a directional sound beam in which the energy is localised close to the axis of propagation [18], and enables us to convert between longitudinal particle velocities ($\mathbf{u}$), and displacements ($\mathbf{U}$) as $\mathbf{u} = \partial\mathbf{U}/\partial\mathbf{t}$. The values X, Y and Z in Eq. (4) are the imposed integration limits. Finally, it is worth noting that the original derivation of Eq. (4) [17] used an inhomogeneous form of the Helmholz equation, the solution of which was simplified using the assumption of $ka \gg 1$. This is equivalent to invoking the parabolic approximation, which was used to derive the well-known KZK equation [19]. Although the two formulations are similar to a greater extent, we use the framework described above as it affords us two advantages. Firstly, it is expressed in three dimensions, as opposed to the two cylindrical coordinates of the KZK scheme, and therefore affords us greater freedom. Secondly, it makes use of an exact solution to the linear Helmholz equation, which is valid for all axial ranges. The first order KZK solution, on the other hand, is not valid for small axial distances $z \lesssim a(ka)^{1/3}$ [20].

2.1. Receiver Correction

Here we describe the correction associated with the integrated response of the receiving transducer. This is the effect previously referred to by Rogers [13] as the diffraction correction, though here we term it the receiver correction. An exact integral expression exists for the receiver correction associated with the linear field when both transmitting and receiving transducers are the same diameter - see Williams (1950) [21]. Based on this, Rogers & Van Buren [13] developed a closed form solution, valid for $(ka)^{1/2} \gg 1$, which was later used by Blackburn & Breazeale [12].

This correction applied only to the fundamental amplitudes. An approximate analytic expression for the correction to the second harmonic amplitudes was presented by Ingenito & Williams [17], and subsequently used by Cobb [22] and Hurley & Fortunko [4].

Here, in order to retain accuracy as far as possible, the receiver correction for the axial second harmonic value is calculated numerically. This is done by computing the transverse amplitude profile associated with the radius of the receiving transducer, integrating over a circle, and then normalising by the area of the circle. This corresponds to the following expression:

$$u_2(0,z) = \frac{1}{\pi b^2} \int_0^b u_2(r,z) 2\pi r dr \tag{7}$$

where b is the radius of the receiving transducer, and $u_2(r,z)$ is computed using equation (4), where $r = \sqrt{(x^2 + y^2)}$.

2.2. Implementation

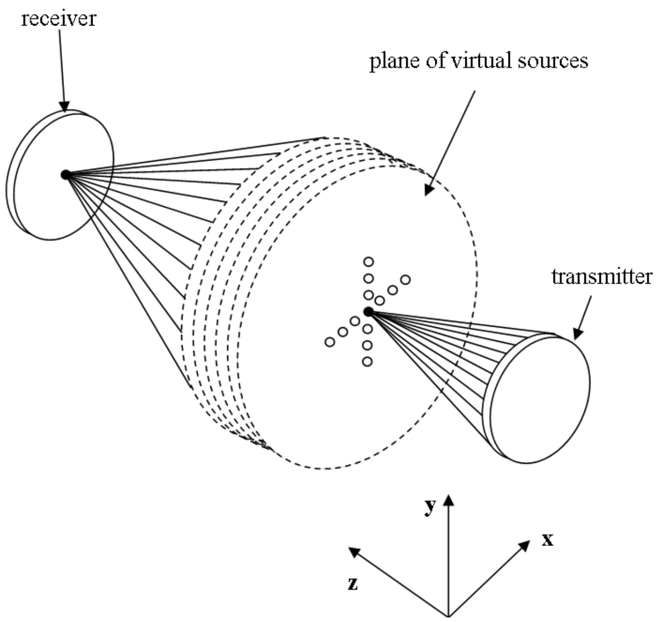

Figure 1: Schematic showing the numerical calculation process. Linear field amplitudes are calculated for each virtual source point (x', y', z') in a circular plane, then squared and propagated on to the target point (x, y, z). This is repeated for all planes parallel to the transducer plane ($z = 0$).

Previously, Ingenito & Williams [17] carried out further theoretical analysis, based on their version of Eq. (4) which was limited to a few special cases. Here the focus is to solve Eq. (4) in as general a manner as possible. To this end, a computer code was written in MATLAB to perform the triple integration numerically. A schematic illustrating the computational process is shown in Fig. 1.

The linear field at any point in the space, $u_1(x', y', z')$, was calculated exactly by using the Rayleigh-Sommerfeld diffraction integral; here we used the algorithm of Zemanek [23] to solve this, adapting it slightly to include a linear attenuation coefficient. This was carried out for all points in a circular slice of the region parallel to the transducer plane. These first-order amplitudes were then squared and, using the appropriate Green's functions, propagated on to the target point. This was then repeated for all slices of the region, and the contributions from all slices were summed. Note that only forward travelling nonlinear contributions were included. That is to say, the virtual sources are assumed only to radiate second harmonic waves in the forwards direction, or the direction of wave propagation. This enabled the axial limit of the integration region to be set equal to the axial distance of the point of interest, $Z = z$, in Eq. (4). Neglecting backscattering in this way is generally thought to be a reasonable assumption, see [17] for a discussion on the matter. Within the parabolic approximation, or assumption of large ka, the linear sound beam is know to be well collimated up to approximately the Rayleigh distance, $r_0 = (1/2)ka^2$, beyond which it diverges spherically. The radial limits on the integration region were therefore imposed a follows: $\sqrt{X^2 + Y^2} = a$ for $z < z_0$; $\sqrt{X^2 + Y^2} = z \tan\theta_b$ for $z > z_0$, where $\theta_b = \tan^{-1}(a/z_0)$ is the approximate beam angle in the far field.

Fig. 2 shows the results of an example simulation. The axial displacement amplitude profiles in a sound beam are calculated with a continuous source excitation of $U_0 = 10^{-9}$m (a typical ultrasonic excitation level), $ka = 40$, and $\beta = 5$. The dashed lines show the effect of integration over a 3mm radius receiver. Note that the receiver tends to smooth much of the oscillatory behaviour in the near field. The trends converge in the far field where the wave fronts become more uniform.

3. Experimental Validation

As a practical test of the model, an experiment was devised to measure the axial variation of fundamental and second harmonic amplitudes in a real sound beam. This involved taking a series of through-transmission measurements on a single sample whilst reducing its length in

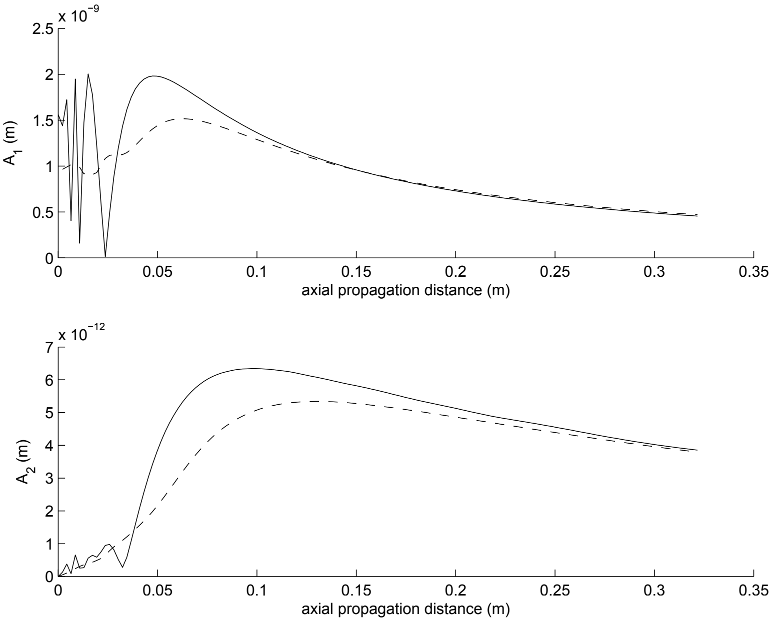

Figure 2: Simulated axial fundamental (top panel) and second harmonic (lower panel) displacement amplitude profiles. Point value trends are shown as solid lines, receiver-corrected trends are shown as dashed lines.

small decrements. A block diagram for the setup is shown in Fig. 3.

The test sample was a cylindrical block of aluminium alloy Al-2011-T3 of length 252mm and radius 44mm. A 16mm diameter PCM41 1.1MHz piezoceramic disc (EP Electronic Components) was bonded using a high strength adhesive to the centre of one end of the sample. Hann-windowed 30-cycle tone burst signals of 3.67MHz, 6.10MHz, and 8.51MHz were generated using a handyscope digital oscilloscope (Tiepie Engineering) and transmitted into the sample via a power amplifier (Amplifier Research, 75A250, 75 Watts). The transmitted signals were recorded at the opposite side of the sample using either a 5- or 10-Mhz wide band receiving probe (Panametrics V310 / V312, 6mm diameter), and fed back to the handyscope for signal processing. After a series of five repeat measurements between which the probe was removed and the surfaces cleaned, a thin (20mm) slice was sawn from the detection end of the sample, and the resulting surface machined to ensure a smooth finish perpendicular to the sides. The measurement process was then repeated. In total, signals were recorded at 12 distances from the source.

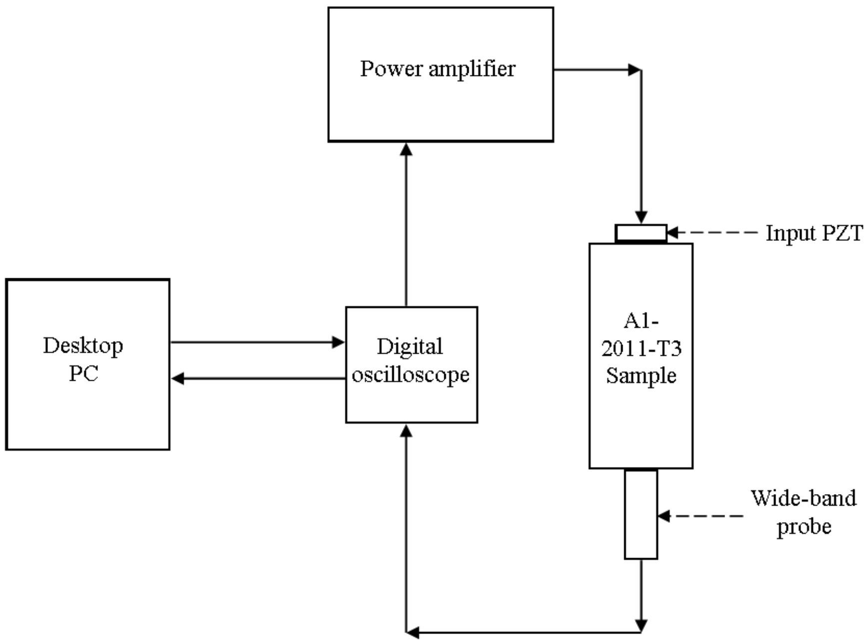

Figure 3: Block diagram for the experimental set up.

3.1. Optimisation

Making nonlinear measurements can be difficult to do reliably. This is particularly the case with solids, as very low levels of nonlinearity and transducer coupling issues can lead to large variability in the results. Therefore, before taking measurements, certain optimisation steps were taken to ensure as much reliability as possible.

A major consideration was minimisation of any nonlinearity at the transmitting source. In an ideal case, a harmonic generation experiment will conform to the boundary condition $u_2(r, 0) = 0$. That is to say, the second harmonic displacement at the source is zero. In reality, however, small amounts of signal distortion may occur along the path to the sample at various stages. Transmission of this spurious nonlinearity could therefore compromise the results. To minimise this effect, two steps were taken. Firstly, the amplifier gain was varied whilst monitoring the nonlinearity, (A_2/A_1^2), of its output directly. By minimising this value, the effective output nonlinearity of the amplifier was reduced. Secondly, the fundamental input frequencies were selected such that the second harmonics coincided with troughs in the PZT's natural frequency response. This 'natural filter' effect is described in more detail by Yan et al. [5].

The next optimisation steps were concerned with the receiving probe, which was coupled to the specimen using a small amount of commercial coupling gel. It was important to ensure that the probe was aligned axially with the centre of the input PZT. This was achieved by transmitting a continuous stream of pulses into the sample, whilst calculating the peak fundamental amplitudes of the signals captured by the probe. By displaying the results in real time, the probe's lateral position could be adjusted to correspond with the field peak. Once in position, a small amount of pressure was applied to the probe to ensure good contact to the specimen surface and minimise the effects of any inhomogeneities in the coupling gel. This receiver coupling process was carried out as carefully as possible, but was inevitably a cause of some degree of variability in the results. A total of five repeat measurements were therefore taken at every distance to establish this variability.

3.2. Amplitude extraction

Certain processing steps were required to extract the amplitudes of the fundamental and second harmonic components, A_1 and A_2, from the digitally recorded raw received signal data. Initially, two digital band pass filters were applied to the raw data to separate the linear and nonlinear signals. The signals were then windowed so as to capture their full length, including the ringing which resulted from exciting the input PZT near a resonance peak. A Fast Fourier Transform (FFT) was then applied to the windowed signals, and the amplitudes were interpolated from the frequency spectrum. In order to account for the shape of the ringing signal, the measured amplitude was scaled by dividing by the mean of the normalised signal envelope (calculated using the Hilbert transform). This correction process is explained and detailed by Liu et al. [11].

3.3. Receiver calibration

The wide band receivers used returned an electrical signal time trace in volts. For the purpose of calculating absolute β, however, the signals were required in the form of amplitude displacements. Although a physical formula exists for calibrating a piezoelectric device in this way (see Dace et al., 1991 [24]), it requires specific knowledge of many parameters which were difficult to measure. Therefore, for the purposes of this paper, the calibration was carried out by taking a series of ultrasonic measurements using the probes, then measuring the same signals using a laser interferometer (Polytec, OFV-505). This enabled a standard conversion from volts to metres at the frequencies of interest. There was, in general, a degree of uncertainty in using this calibration method, but here we are not so interested in the precise value of β measured, as in the effect of the method used to extract it. The calibration values are therefore only of secondary concern.

4. Results

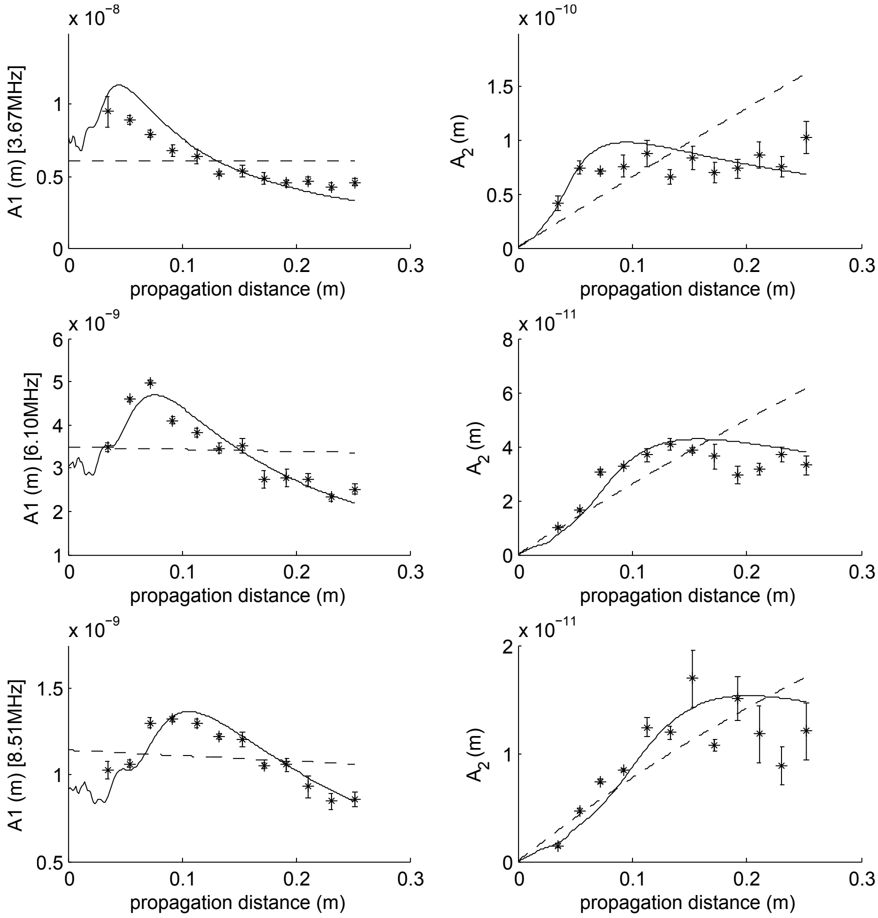

Figure 4: Axial amplitude profiles: experiment (starred points) vs simulation (solid lines) and plane wave prediction (dashed lines). Error bars on the experimental data represent the standard deviation of five repeat measurements

Fig. 4 shows a comparison of the experimental data with theoretical trends generated using the simulation described in Section 2. Also included are trends calculated based on the plane wave theory. The left hand panels show the variation of the fundamental amplitudes at the three input frequencies used, while the right hand panels show that of the corresponding second harmonic amplitudes.

4.1. Theoretical trends

Both sets of theoretical trends were calculated by matching the model parameters with those known from the experiment. However, one parameter which was not known, and which could not easily be measured, was the attenuation coefficient, α. As a best estimate, we took its value to be 0.4Npm^{-1} at a frequency of 10MHz in accordance with Ref. [25], and adopted a simple viscous damping law, such that:

$$\alpha_f = 0.4\left(\frac{f}{10}\right)^2 \tag{8}$$

where α_f is the is the attenuation coefficient at frequency f (in MHz). This was subsequently used in all theoretical calculations; we discuss the importance of the precise attenuation values in due course.

4.1.1. Plane wave trends

The plane wave trends, shown as the dashed lines in Fig. 4, were calculated using the damped expressions for A_1 and A_2 corresponding to Eq. 3 [18]:

$$|A_1(z)| = u_0 e^{-\alpha z}; \qquad |A_2(z)| = \frac{k^2 u_0^2 \beta}{8\alpha}(e^{-2\alpha z} - e^{-4\alpha z}) \tag{9}$$

where z is the axial propagation distance, and u_0 is the linear displacement amplitude of the transmitter. Note that this was not known, but for the purposes of the trends shown, it was calculated so as to provide a mean best fit to the experimental data. The A_2 plane wave trends use the mean value of β, found by using Eq. 3 with all experimental data points. It is noted that due to the low damping values, both sets of A_1 and A_2 plane wave trends show only a slight curvature with respect to the would-be horizontal and linearly increasing lines expected for zero damping.

4.1.2. Simulated trends

For the simulated trends (solid lines in Fig. 4), the curve-fitting approach was much the same, in that the mean best fit to the experimental data was sought. The simulation was run with a fundamental input amplitude of 1, then the ratio of the observed and predicted A_1 values was calculated. This gave a theoretical source amplitude corresponding to each experimental data point at distance z:

$$u_0(z) = \frac{A_{1,exp}(z)}{A_{1,sim}(z)} \tag{10}$$

The simulated A_1 profile shown in Fig. 4 is scaled using the mean of all such $u_0(z)$. Running the simulation with $u_{0,sim} = 1$ and $\beta_{sim} = 1$ enabled the experimental absolute β values to be calculated as:

$$\beta(z) = \frac{A^2_{1,sim}(z)}{A_{2,sim}(z)} \left(\frac{A_{2,exp}(z)}{A^2_{1,exp}(z)} \right) \tag{11}$$

The simulated second harmonic profiles shown in figure (4) are scaled using the mean value of all $\beta(z)$. All β values calculated in this manner are plotted later as a function of axial distance (see Fig. 6).

4.1.3. Attenuation value

While attenuation in aluminium is known to be low, we now assess the effects of the uncertainty in the parameter. In Fig. 5, we include receiver-corrected A_1 and A_2 trends, calculated for the frequencies shown in Fig. 4, now with damping levels which vary between 0 - 200% of those used previously. The A_1 trends are scaled to the un-damped case ($\alpha = 0$), and the A_2 trends are scaled by the square of the same factor. It can be seen that in this range of relatively low damping values around that used, the A_1 trends are barely separable. The A_2 trends show slightly more variation, more so at the higher frequencies, but here the experimental error bars in the data shown in Fig. 4 are correspondingly larger. Due to this, altering the damping level is unlikely to affect the fit to the experimental data.

4.2. Experimental data

At this stage, the main observation from Fig. 4 is that the plane wave trends fall short of recreating the observed experimental data, while the simulated trends provide a reasonable level of agreement. The deviation between simulation and experiment, in particular with regards to the second harmonic trends, is most likely due to the inherent difficulties associated with making measurements in solids; the measures intended to overcome these were described in section 3.1. An interesting comparison can be made here with the work of Cobb (1983) [22], who made similar axial pressure measurements, but using fluid nonlinear media.

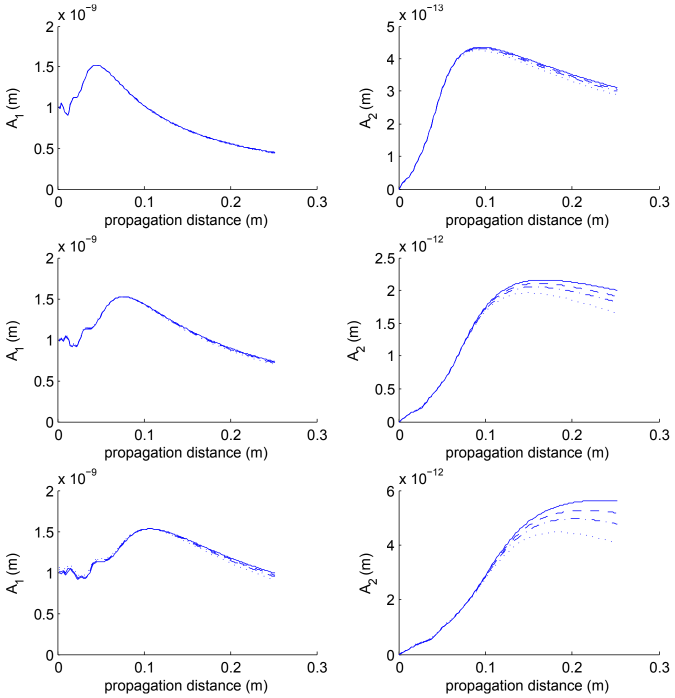

Figure 5: Receiver-corrected axial amplitude trends with varying levels of damping. In each case, the attenuation law follows $\alpha_f = \alpha_0(f/10\text{MHz})^2$, where $\alpha_0 = 0$ (solid lines); 0.2 (dashed lines), 0.4 (dot-dashed lines) and 0.8 (dotted lines).

A theoretical consideration is that the input signals were not continuous sinusoids, as is assumed for the theoretical trends, but were in fact bursts of finite length. Extending the simulation to account for this excitation time-variability is possible, but would dramatically increase the computation time. As a compromise, the bursts were intentionally generated with a relatively large number of cycles to better approximate a continuous wave pressure field. Presumably, however, this approximation cannot be ignored as a potential contributing factor to the observed discrepancies.

5. Discussion

Fig. 6 shows both the β' (i.e., A_2/A_1^2) values (left hand panels) and absolute β values, extracted using the plane wave- and simulation-based approaches, as a function of axial distance (right hand panels). The plane wave-derived absolute β values (dashed lines) are calculated using Eq. (3); the simulation-derived values (solid lines) as discussed previously, using equation (11).

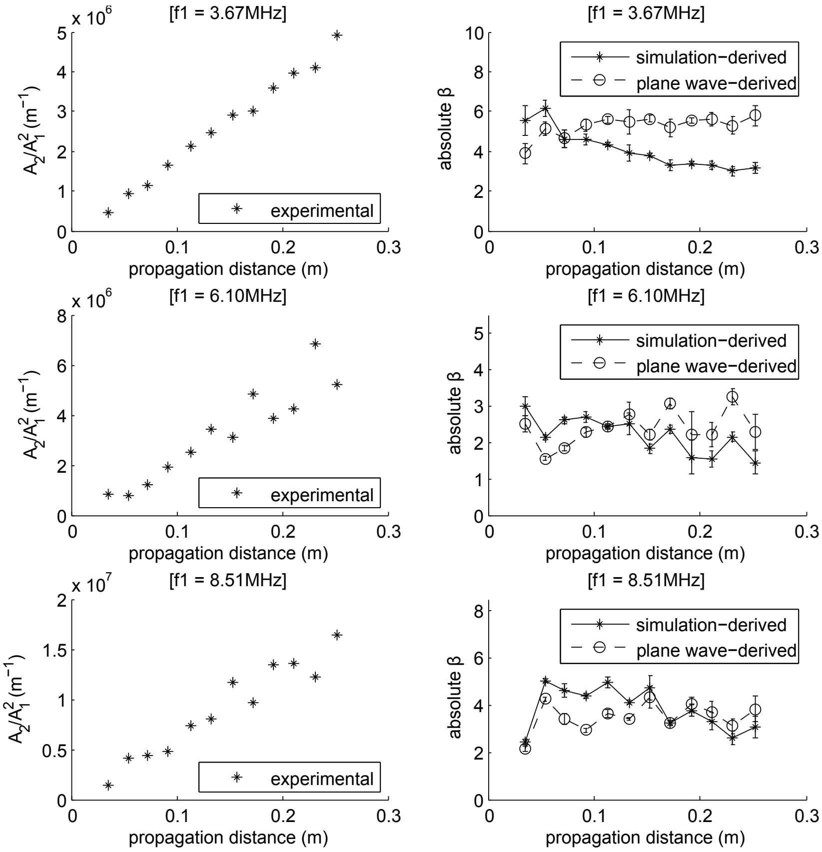

Figure 6: Axial variation of absolute β, calculated using both the simulation and the plane wave theory.

Firstly, it is interesting to note that the β' values show a tendency to increase linearly with propagation distance. This fact is predicted by the plane wave model, but can also be explained by considering the generation and decay mechanisms in three dimensions. It is therefore not necessarily indicative of plane wave behaviour. Looking at the extracted absolute β values, it is evident that neither method shows more of a tendency to produce a consistent β value than the other. However, it is clear from Fig. 4 that the simulation predicts the axial variation of the A_1 and A_2 trends more accurately than the plane wave model. The fact that no identifiable improvement is seen in the consistency of the β values shown in Fig. 6 must therefore be due to the variability in the experimental data, which effectively masks the differences between the trends. Under closer scrutiny, consistent features can be noticed between the subplots. Specifically, the trends return different values in the near field, then coincide briefly, before diverging again.

These features can be seen more clearly when we consider the idealised case. That is, one in which the experimental results conform exactly to the predicted trends of the simulation. To illustrate this, we use the simulated trends shown in Fig. 4 as a theoretical set of data, and the plane wave expression is then used to extract the absolute β profiles as a function of axial distance. The results are shown in Fig. 7. The solid lines are calculated using the damped plane wave result, Eq. (3), while the dot-dashed lines use the undamped result, equation (2). The actual input value, $\beta = 1$, is included as a horizontal dashed line for reference.

The consistent features are now more apparent between the three subplots. In the near field, the extracted values fluctuate somewhat, reach a minimum, and then rise to coincide with the true value before continuing to diverge. The presence of the dip in the near field region is significant, as it offers an indication of the limitations of the common assumption of an approximately planar near field region. Here the underestimation of β is more significant at higher frequencies, as indicated by the slightly more pronounced dip. The distance at which the trends coincide, in each case, is around $0.6r_0$, where $r_0 = (1/2)ka^2$ is the Rayleigh distance. Further out, it is known that the beam is characterised by spherically diverging waves, and here we expect the plane wave measurement to return diverging β values as shown. These features are also apparent to a certain extent in Fig. 6, where the real experimental data are used. Notably, both Fig. 6 and Fig. 7 indicate that the plane wave measurement overestimates β by a factor of almost 2 at the maximum axial distance when the lower input frequency of 3.67MHz is used. The corresponding value when the higher frequency, 8.51MHz is used is much less, around 20%. The neglect of attenuation seems to produce a small deviation in the extracted β value in Fig. 7, which is consistent with the small attenuation values in aluminium. However, this will be of greater concern in materials such as steel, where the attenuation values are known to be much larger.

As a final remark, we refer to the actual values of extracted β, as shown in Fig. 6. As mentioned previously, the calibration procedure was subject to a significant degree of uncertainty, meaning the values indicated are not precise. What is more, each frequency used corresponds to a slightly different value. We note, however, that all the values fall within the approximate range 1-6, which agrees with values published in the literature for measurements on similar aluminium alloys - see for example [26, 27, 28].

6. Conclusion

In this paper we have investigated the importance of certain features of a typical nonlinear measurement which are generally overlooked when calculating absolute β. We have described a numerical model of bulk harmonic generation which captures the effects of diffraction, attenuation and nonlinearity in a sound beam. The additional effects of receiver integration were incorporated to provide a full representation of a typical practical measurement. Upon comparison with experimental data, the simulation was found to be a significant improvement on the plane wave model as a predictor of axial fundamental and second harmonic amplitude profiles. This, however, apparently did not translate into an immediately obvious improvement in extracted values of absolute β. It was suggested that this fact was due in large part to the variability in the experimental data, something which is a problem typical to nonlinear measurements in solids. As an alternative consideration, a calculation was presented of the plane-wave extracted absolute β values based on idealised (simulated) data. Here it was seen that, in the near field, the plane wave based correction oscillates, at points underestimating β by a factor of up to 40% at the highest frequency used here, and around 25 % at the lowest frequency. The importance of this result, to some extent, depends on both the level of precision required, and that available. On one hand, an improvement of 40% in a measurement of β may represent a critical difference in the amount of damage suspected in a component. On the other hand, the experimental data shown here, for example, exhibit a degree of variability which is comparable with the suspected inaccuracy in using the plane wave measurement. At large axial distances, the result is more clear-cut. In this region the plane wave value diverges from the true value due to its neglect of spreading in the acoustic field. The effect is particularly pronounced at the lowest frequency tested, where β is overestimated by around 80% at the largest axial distance. It is therefore apparent that care should be taken when measuring β using the plane wave correction at large distances, especially when using low input frequencies. Additionally, it is noted that attenuation should not be overlooked when measuring β in highly attenuating materials.

7. Acknowledgement

This work was funded by the UK Engineering and Physical Sciences Research Council (EPSRC), grant number EP/I003207/1.

References

[1] R. T. Beyer, Nonlinear Acoustics, Chapter 2: 'The Parameter B/A', Academic Press, 1998.

[2] L. D. Landau, E. M. Lifshitz, Theory of Elasticity, vol. 7 of Course of Theoretical Physics, Pergamon Press, 2nd edition, 1970.

[3] L. K. Zarembo, V. A. Krasil'nikov, Nonlinear phenomena in the propagation of elastic waves in solids, Soviet Physics Uspekhi 13 (1971) 778.

[4] D. C. Hurley, C. M. Fortunko, Determination of the nonlinear ultrasonic parameter beta using a michelson interferometer, Meas. Sci. Technol. 8 (1997) 634 – 642.

[5] D. Yan, B. W. Drinkwater, S. A. Neild, Measurement of the ultrasonic nonlinearity of kissing bonds in adhesive joints, NDT & E International 42 (2009) 459 – 466.

[6] C. Pantea, C. F. Osterhoudt, D. N. Sinha, Determination of acoustical nonlinear parameter β of water using the finite amplitude method, Ultrasonics (2013), http://dx.doi.org/10.1016/j.ultras.2013.01.008 (????).

[7] S. Baby, B. N. Kowmudi, C. M. Omprakash, D. V. V. Satyanarayana, K. Balasubramaniam, V. Kumar, Creep damage assessment in titanium alloy using a nonlinear ultrasonic technique, Scripta Materialia 59 (2008) 818–821.

[8] J.-Y. Kim, L. J. Jacobs, J. Qu, J. W. Littles, Experimental characterization of fatigue damage in a nickel-base superalloy using nonlinear ultrasonic waves, Journal of the Acoustical Society of America 120 (2006) 1266–1273.

[9] A. Kumar, C. J. Torbet, J. W. Jones, T. M. Pollock, Nonlinear ultrasonics for in situ damage detection during high frequency fatigue, Journal of Applied Physics 106 (2009).

[10] K.-Y. Jhang, K.-C. Kim, Evaluation of material degradation using nonlinear acoustic effect, Ultrasonics 37 (1999) 39–44.

[11] S. Liu, S. Best, A. J. Croxford, S. A. Neild, Measuring bulk nonlinearity using harmonic generation, NDT&E International (2012).

[12] B. D. Blackburn, M. A. Breazeale, Nonlinear distortion of ultrasonic waves in small crystalline samples, The Journal of the Acoustical Society of America 76 (1984) 1755–1760.

[13] P. H. Rogers, A. L. Van Buren, An exact expression for the lommel-diffraction correction integral, The Journal of the Acoustical Society of America 55 (1974) 724–728.

[14] V. Labat, J. P. Remenieras, O. Bou Matar, A. Ouahabi, F. Patat, Harmonic propagation of finite amplitude sound beams: experimental determination of the nonlinearity parameter b/a, Ultrasonics 38 (2000) 292 – 296.

[15] F. Chavrier, C. Lafon, A. Birer, C. Barriere, X. Jacob, D. Cathignol, Determination of the nonlinear parameter by propagating and modeling finite amplitude plane waves, The Journal of the Acoustical Society of America 119 (2006) 2639–2644.

[16] V. P. Kuznetsov, Equations of nonlinear acoustics, Sov. Phys. Acoust 16 (1971) 467–470.

[17] F. Ingenito, A. O. Williams Jr, Calculation of second-harmonic generation in a piston beam, The Journal of the Acoustical Society of America 49 (1971) 319–328.

[18] A. N. Norris, Nonlinear Acoustics, Chapter 9: 'Finite-Amplitude Waves in Solids', Academic Press, 2008.

[19] J. Berntsen, J. N. Tjotta, S. Tjotta, Nearfield of a large acoustic transducer. part iv: Second harmonic and sum frequency radiation, The Journal of the Acoustical Society of America 75 (1984) 1383–1391.

[20] V. E. Kunitsyn, O. V. Rudenko, Second-harmonic generation in the field of a piston radiator, Sov. Phys. Acoust. 24 (1978) 310–313.

[21] A. O. Williams Jr, The piston source at high frequencies, The Journal of the Acoustical Society of America 23 (1951) 1–6.

[22] W. N. Cobb, Finite amplitude method for the determination of the acoustic nonlinearity parameter b/a, The Journal of the Acoustical Society of America 73 (1983) 1525–1531.

[23] J. Zemanek, Beam behavior within the nearfield of a vibrating piston, The Journal of the Acoustical Society of America 49 (1971) 181–191.

[24] G. E. Dace, R. B. Thompson, O. Buck, Measurement of the acoustic harmonic generation for materials characterization using contact transducers, Review of progress in quantitative nondestructive evaluation 11B (1991).

[25] Tables of Physical & Chemical Constants (16th edition 1995), Kaye & Laby Online Version 1.0 (2005).

[26] J. Cantrell, W. Yost, Nonlinear ultrasonic characterization of fatigue microstructures, International Journal of Fatigue 23, Supplement 1 (2001) 487 – 490.

[27] W. T. Yost, J. H. Cantrell, The effects of artificial aging of aluminum 2024 on its nonlinearity parameter, Review of Progress in Quantitative Nondestructive Evaluation 12 (1993) 2067–2067.

[28] J. H. Cantrell, K. Salama, Acoustoelastic characterisation of materials, International Materials Reviews 36 (1991) 125 – 145.

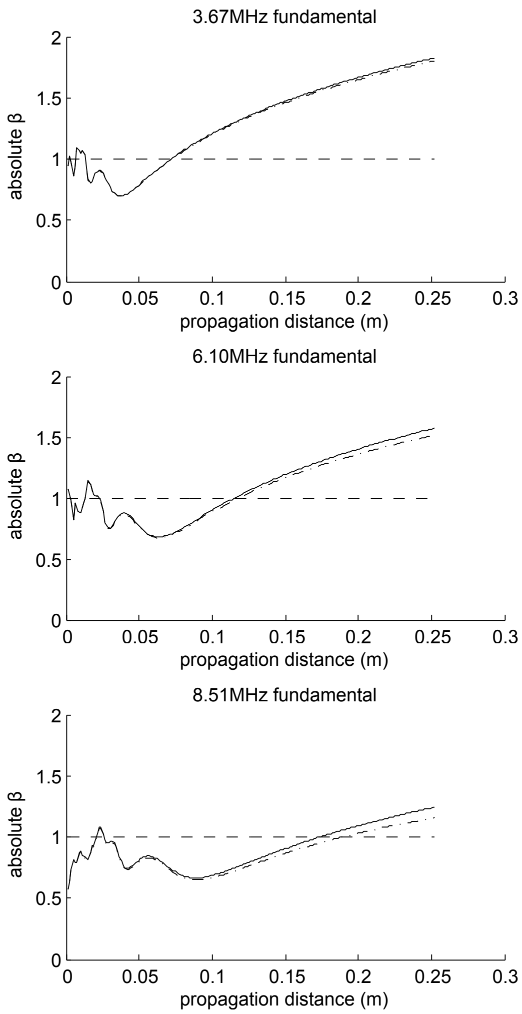

Figure 7: Theoretical axial variation of absolute β calculated using the plane wave theory. Undamped calculations are shown as dashed lines, damped calculations as solid lines. The calculations are based on idealised axial A_1 and A_2 data generated using the simulation.